Supporting Information

Lightly Fluorinated Graphene as a Protective Layer for n-Type Si(111) Photoanodes in Aqueous Electrolytes

Adam C. Nielander[‡,a], Annelise C. Thompson[‡,a], Christopher W. Roske[a], Jacqueline A. Maslyn[a], Yufeng Hao[b], Noah T. Plymale[a], James Hone[b], and Nathan S. Lewis[a,]*

[‡]*These authors contributed equally to this work.*

[a]Division of Chemistry and Chemical Engineering, California Institute of Technology, Pasadena, CA, 91125, United States

[b]Department of Mechanical Engineering, Columbia University, New York, New York, 10027, United States

*Corresponding author: nslewis@caltech.edu

Contents

I. Methods

Materials

Single-crystalline, Czochralski grown, (111)-oriented, planar, 380 μm thick, phosphorus doped, 1.1 Ω-cm resistivity (doping density, $N_D \approx 5x10^{15}$ cm^{-3}) single-side polished n-type silicon wafers were obtained from University Wafer, Inc. Single-crystalline, (100)-oriented, planar, 380 μm thick, boron doped, 1-10 Ω-cm resistivity single-side polished p-type silicon wafers with 300 nm thermal oxide (SiO_2 on Si substrate) were also obtained from University Wafer, Inc. Silicon wafers with an np^+ homojunction (np^+-Si) was fabricated using a previously reported procedure (Yang et. al) via room temperature ion implantation on n-Si at a 7° incident angle using ^{11}B accelerated to 45 keV with a dose of 1×10^{14} cm^{-2}, and then at 32 keV with a dose of 5×10^{14} cm^{-2}.[1] The back sides of the wafers were implanted with ^{31}P at 140 keV with a dose of 1×10^{14} cm^{-2}, and then at 75 keV with a dose of 5×10^{14} cm^{-2} in order to reduce contact resistance. Dopant activation, both for the junction p^+ layer and the back-surface field (BSF) n^+ layer, was achieved via rapid thermal annealing at 1000 °C for 15 s under a flow of $N_2(g)$.

Water was obtained from a Barnstead Nanopure system and had a resistivity ≥ 18.0 MΩ-cm. Copper Etch Type CE – 100 ($FeCl_3$-based, Transene Company, Inc., Danvers, MA), and buffered HF improved (aq) (semiconductor grade, Transene Company, Inc.) were used as received. Acetone (HPLC grade, Sigma-Aldrich) was used as received. Acetonitrile (99.8% anhydrous, Sigma-Aldrich) used in electrochemical measurements was dried over 4A molecular sieves prior to use.

Ferrocene (Fc, bis(cyclopentadienyl)iron(II), 99%, Strem), cobaltocene ($CoCp_2$, bis(cyclopentadienyl)cobalt(II), 98%, Strem), and acetylferrocene (AcFc, (acetylcyclopentadienyl)-cyclopentadienyl iron(II), 99.5%, Strem) were purified via sublimation.

Ferrocenium tetrafluoroborate ($Fc^+[BF_4]^-$, bis(cyclopentadienyl)iron(III) tetrafluoroborate, technical grade, Sigma-Aldrich) was recrystallized from a mixture of diethyl ether (ACS grade, EMD) and acetonitrile (ACS grade, EMD) and dried under vacuum. Cobaltocenium hexafluorophosphate ($CoCp_2^+$, bis(cyclopentadienyl)cobalt(III) hexafluorophosphate, 98%, Sigma-Aldrich) was recrystallized from a mixture of ethanol (ACS grade, EMD) and acetonitrile (ACS grade, EMD) and dried under vacuum. Acetylferrocenium ($AcFc^+$) was generated in situ via electrochemical oxidation of $AcFc^0$ with the concomitant reduction reaction occurring in a compartment that was separated by a Vycor frit from the working electrode compartment. Potassium ferricyanide ($K_3[Fe(CN)_6]$, 99.2%, Sigma-Aldrich) and potassium ferrocyanide ($K_4[Fe(CN)_6]\bullet 3H_2O$, ACS Certified, Fisher Scientific) were used as received. $LiClO_4$ (battery grade, Sigma-Aldrich) was used as received. Petri dishes used were Falcon Optilux™ branded and were cleaned with water prior to use. All other chemicals were used as received unless otherwise noted.

Electrode/Sample fabrication

Monolayer graphene was grown by chemical vapor deposition (CVD) of carbon on Cu using previously reported methods.[2] Additional CVD-grown monolayer graphene on Cu was purchased from Advanced Chemical Supplier Materials (Medford, MA).

A 2.5 cm x 1 cm piece of monolayer graphene on Cu (from either source) was fluorinated using a home-built XeF_2 pulse chamber, with one pulse of XeF_2 (g) at 2 Torr for 90 s with a base pressure of <1 mTorr. The fluorinated graphene samples on Cu were then coated with 495K A4 polymethyl methacrylate (PMMA, MicroChem) by spincoating at 2000 rpm (500 rpm s^{-1} acceleration) for 60 s, followed by a 5 min bake at 185 °C. This procedure was repeated twice to

increase the PMMA thickness. This process yielded a PMMA/F–Gr/Cu stack. PMMA/Gr/Cu stacks were obtained using nominally the same spin coating method but without graphene exposure to XeF_2.

Smaller pieces were cut from the PMMA/F–Gr/Cu and floated in $FeCl_3$ solution until complete removal of the Cu (~1 h) was observed. To remove etchant residue, each stack was transferred between five consecutive ≥18MΩ-cm resistivity water baths. N-type Si was etched for 30 s in buffered HF improved to yield n-Si–H surfaces. SiO_2 on Si substrates were cleaned using a modified SC-1/SC-2 cleaning method. SC-1 consisted of soaking the Si wafers in a 5:1:1 (by volume) solution of H_2O, NH_4OH (~30 wt.%, J.T. Baker) and H_2O_2 (~35 wt.%, Sigma) for 10 min at 75 °C. After washing with H_2O, SC-1 cleaned wafers were exposed to SC-2 conditions, which consisted of soaking the Si wafers in a 5:1:1 (by volume) solution of H_2O, HCl (11.1 M, Sigma) and H_2O_2 (~35 wt.%, Sigma) for 10 min at 75 °C. A clean PMMA/F–Gr stack was then transferred gently onto the appropriately prepared Si wafer (buffered HF etched Si for electrode fabrication, SC-1/SC-2 cleaned SiO_2 on Si substrate for chemical stability interrogation via Raman spectroscopy) from the water bath and dried with a stream of $N_2(g)$ to remove any remaining water between the Si wafer and the graphene sheet. The final PMMA/F–Gr/wafer stack was baked at 80 °C for 10 min in air. The majority of the PMMA was detached with a 10 min acetone soak and the remaining PMMA residue was removed by an anneal (H_2:Ar v:v 5:95) for 2h at 350 °C, leaving an F–Gr/Si stack.[3] Gr/Si stacks were prepared by nominally identical procedures using pristine graphene. Generally, 5-10 electrodes were made at the same time from the same PMMA/F–Gr/Cu or PMMA/Gr/Cu stack, respectively.

N-Si/F–Gr electrodes were fabricated using Ga:In (75:25) eutectic as an ohmic back contact. The wafers were attached to a Cu wire with Ag paint (high purity, SPI Supplies). All

surfaces except the F–Gr layer were covered with insulating epoxy (Loctite Hysol 9460). Monolayer graphene-covered Si(111) electrodes were fabricated using an analogous procedure in which all of the above steps were executed with the exception that the graphene was not exposed to the XeF_2 (g). CH_3-terminated Si(111) wafers were prepared using a previously reported procedure and were not etched with HF prior to use in electrode fabrication.[4] Graphene-free, hydride terminated Si(111) electrodes (n-Si–H and np^+-Si–H) were etched with buffered HF(aq) immediately before use.

Instrumentation

X-ray photoelectron spectroscopic (XPS) data were collected at ~5×10^{-9} Torr using a Kratos AXIS Ultra DLD with a magnetic immersion lens that consisted of a spherical mirror and concentric hemispherical analyzers with a delay-line detector (DLD). An Al Kα (1.486 KeV) monochromatic source was used for X-ray excitation. Ejected electrons were collected at a 90° angle from the horizontal. The CASA XPS software package v 2.3.16 was used to analyze the collected data.

Raman spectra were collected with a Renishaw Raman microscope at λ=532 nm through an objective with numerical aperture=0.75. The laser power was ~ 3 mW.

UV/Vis transmission spectra were collected with a Cary 5000 absorption spectrometer equipped with an external DRA 1800 attachment. The data were automatically zero/baseline corrected by the instrument before any additional processing was performed.

Scanning electron microscope (SEM) images were obtained using a FEI Nova NanoSEM 450 at an accelerating voltage of 10.00 kV with a working distance of 5 mm and an in-lens secondary electron detector.

Electrochemical data were obtained using a Princeton Applied Research Model 273, Biologic SP-250, or a Gamry Reference 600 potentiostat. A Pt wire reference electrode (0.5 mm dia., 99.99% trace metals basis, Sigma-Aldrich) and a Pt mesh counter electrode (100 mesh, 99.9% trace metals basis, Sigma-Aldrich) were used for the electrochemical measurements. The cell potentials for the nonaqueous redox species were determined using cyclic voltammetry to compare the solution potential to the formal potential of the redox species. The potential difference between electrolyte solutions was calculated using the difference between the solution potentials for each redox couple in conjunction with previously reported standard formal

reduction potentials [$E^{o'}(CoCp_2^{+/0})$ = -1.33 vs. $E^{o'}(Fc^{+/0})$; $E^{o'}(AcFc^{+/0})$ =+0.26 vs. $E^{o'}(Fc^{+/0})$] . The CH_3CN-$CoCp_2^{+/0}$ solution ($CoCp_2$ [3 mM]/ $CoCp_2^+$ [50 mM]) was calculated to have a solution potential of $E(A/A^-)$ = -1.26 V vs. Fc/Fc^+, the CH_3CN-$Fc^{+/0}$ solution (Fc [55 mM]/ Fc^+ [3 mM]) was calculated to have $E(A/A^-)$ = -0.10 V vs. Fc^+/Fc, and the CH_3CN-$AcFc^{+/0}$ solution (pre-electrolysis AcFc concentration = [50 mM]) was calculated to have $E(A/A^-)$ = +0.40 V vs. Fc^+/Fc. The nonaqueous electrolyte solutions each contained 1.0 M $LiClO_4$. The aqueous 50 mM $K_3[Fe(CN)_6]$ - 350 mM $K_4[Fe(CN)_6]$ solution contained no additional supporting electrolyte due to the high intrinsic salt concentration. The current under forward bias saturated at much larger values in the $Fe(CN)_6^{3-/4-}$ solution than in the Fc^+/Fc solution due to the increased concentration of electron-accepting species in the $Fe(CN)_6^{3-/4-}$ solution. The electrolyte solution was rapidly stirred with a small, Teflon-covered stir bar. Illumination was provided with an ENH-type tungsten-halogen lamp. Illumination intensities were set to provide ~10-11 mA cm^{-2} of light-limited current density. These intensities corresponded to ~1/3rd Sun at AM 1.5G (~33 mW cm^{-2}), respectively, as determined through the concurrent use of a Si photodiode (Thor Laboratories) that was calibrated relative to a secondary standard photodetector that was NIST-traceable and calibrated at 100 mW cm^{-2} of AM1.5G illumination. Nonaqueous electrochemistry was performed anaerobically in an Ar(*g*)-filled glovebox. Aqueous electrochemistry was performed in air. Electrodes were washed with H_2O and dried prior to transfer between electrolyte solutions. Plots of current density vs. time data were smoothed using a 9 point Savitzky-Golay algorithm via data analysis software (Igor Pro 6). Normalized current density was calculated by multiplying the ratio of the light intensity at a time point of interest to the light intensity at t=0 s by the original current density and dividing the resulting value by the current density measured at the time point of interest.

The current density versus potential data in HBr(aq) were measured using a three-electrode setup with a Si working electrode, a Pt wire pseudo-reference electrode, and a large Pt mesh counter electrode. The electrolyte consisted of aqueous 0.4M Br_2 - 7.0 M HBr (pH=0) electrolyte under rapid stirring, and ~33 mW cm^{-2} of simulated solar illumination from an ELH-type W-halogen lamp.

Photoelectrochemical deposition of Pt was performed by immersing the electrode into an aqueous solution of 5 mM K_2PtCl_4 (99.9%, Alfa Aesar) and 200 mM LiCl. Using a three-electrode setup, with a saturated calomel reference electrode and a Pt mesh counter electrode, galvanostatic control was maintained at -0.1 mA/cm^2 in a stirred solution until -100 mC/cm^2 had passed. The samples were then rinsed with deionized water and were dried under a stream of $N_2(g)$.

II. Supporting Data

Electrochemical behavior of np$^+$-Si/F–Gr electrodes in aqueous solution

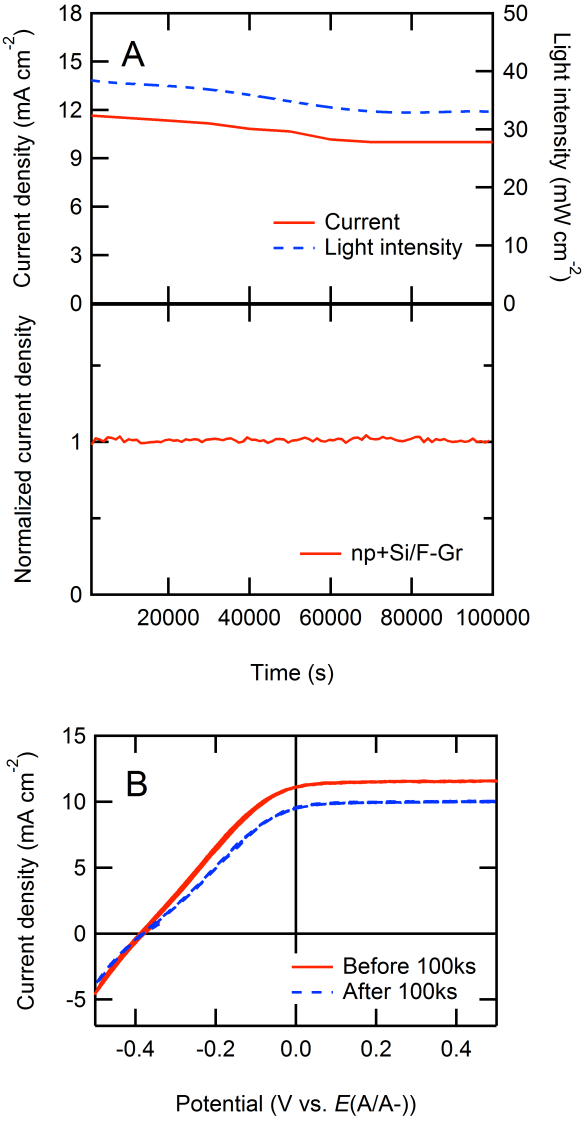

Figure S1. Current density vs. time (*J*-*t*) and current density vs. potential (*J*-*E*) behavior of np$^+$-Si/F–Gr electrodes in contact with aqueous 50 mM $Fe(CN)_6^{3-}$ - 350 mM $Fe(CN)_6^{4-}$ electrolyte under ~33 mW cm^{-2} of ENH-type W-halogen illumination. (A) The *J*-t behavior of np$^+$-Si/F–Gr at *E*= 0 V vs. *E*(A/A$^-$) over 100,000 s (>24 h). The normalized current density is reported to

correct for variations in the light intensity during the experiment. (B) *J*-*E* behavior of np^+-Si/F–Gr (3 scans at 50 mV s^{-1}) before and after exposure to the conditions depicted in (A). The current density decay in the original chronoamperograms is consistently ascribed to fluctuations in the light source, as well as to decomposition of the $Fe(CN)_6^{3-/4-}$ under illumination, which produced thin colored film on the electrochemical cell over the course of the experiment depicted in (A).

Comparison of graphene-imparted stability between graphene and fluorinated graphene electrodes

The photoelectrochemical stability of pristine graphene-coated n-Si electrodes and of fluorinated graphene-coated electrodes was tested by collecting *J-t* data for n-Si/Gr and n-Si/F–Gr electrodes from four different electrode 'batches' (two Gr/n-Si and two F–Gr/Gr batches) in contact with aqueous 50 mM $Fe(CN)_6^{3-}$ - 350 mM $Fe(CN)_6^{4-}$ under ~33 mW cm^{-2} of ENH-type W-halogen illumination (Figure S2). These batches of electrodes each mutually consisted of 5-6 electrodes in which each electrode was fabricated from the same section of a larger sheet of Gr or F–Gr, respectively. However, between batches of electrodes, different PMMA/(F–)Gr/Cu stacks or different regions of the same stack were used. The n-Si/Gr from the first graphene electrode batch (batch Gr_A) exhibited stable current densities for > 1000 s (Figure S2A). Among these electrodes fabricated, all five electrodes were photoelectrochemically stable (5/5 stable, where stability was defined as having a current density at *t*=1000 s of at least 60% of the current density displayed at *t*=0 s. This definition was used because some graphene-covered (and F–Gr covered) electrodes displayed an initial decay of current density followed by a subsequent stabilization, as seen in Figure S3. This behavior is consistent with the hypothesis that any pinholes in the graphene protective coating led to the oxidation at the exposed Si surface, but that stability is observed when the exposed Si is passivated with SiO_x. However, the other batch (batch Gr_C, Figure S2C) yielded only two n-Si/Gr electrodes out of six that exhibited stable current densities for > 1000 s (2/6 stable). The inconsistent behavior in the photoelectrochemical stability imparted by pristine graphene coatings on n-Si electrode was observed over many iterations of graphene growth and electrode fabrication. Conversely, both batches of F–Gr coated n-Si electrodes (batch F-Gr_B, Figure S2B and batch F-Gr_D, Figure S2D) yielded n-Si/F–Gr

electrodes that exhibited stable current densities for > 1000 s (5/5 stable in batch F-Gr_B and 5/5 stable in batch F-Gr_D). The improved consistency of the photoelectrochemical stability is one of the key attributes of the fluorinated graphene-coated n-Si electrodes relative to the routinely observed behavior of pristine graphene-coated n-Si electrodes.

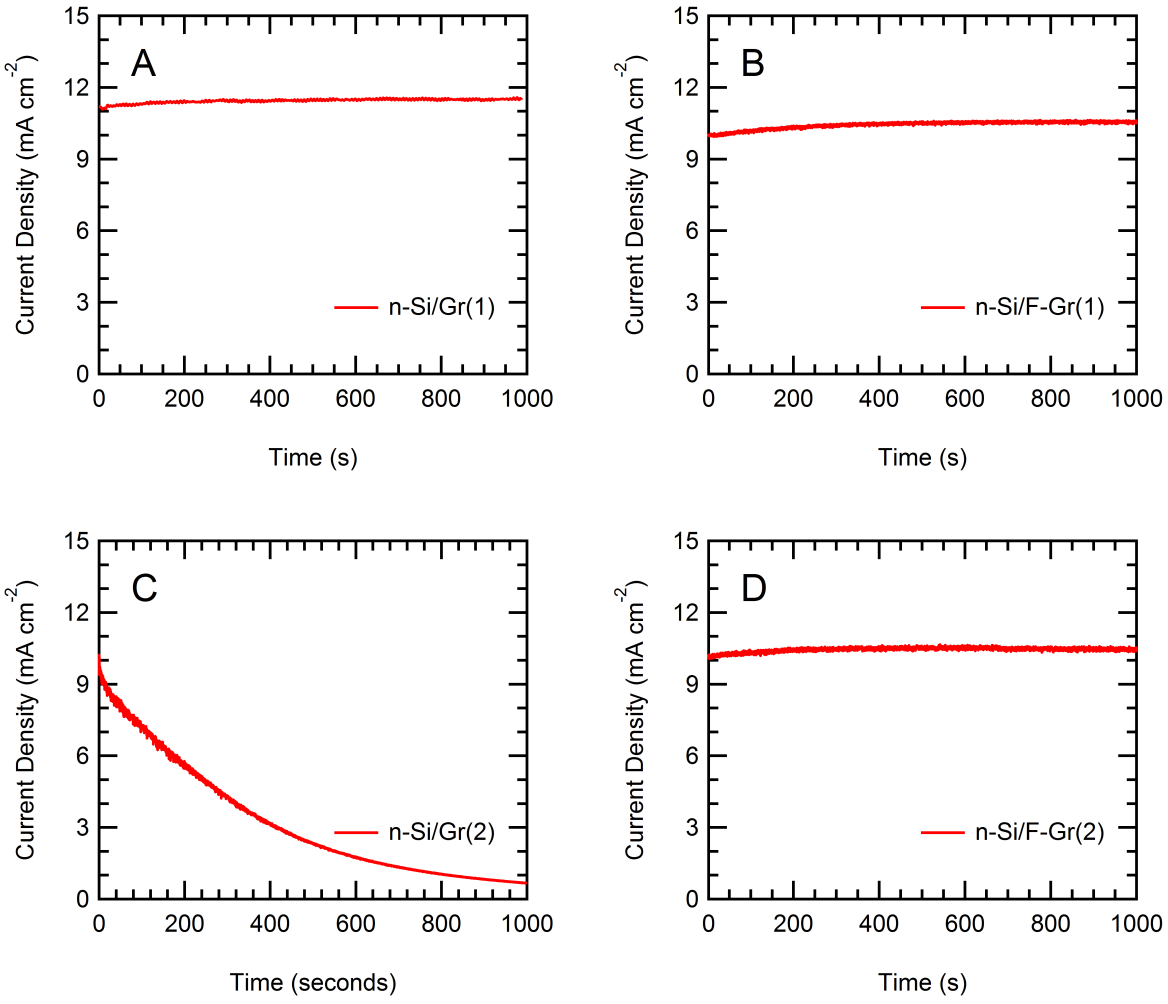

Figure S2. Representative *J-t* data for n-Si/Gr and n-Si/F–Gr electrodes from four different electrode batches (two Gr/n-Si and two F–Gr/Gr batches, see above) in contact with aqueous 50 mM $Fe(CN)_6^{3-}$ - 350 mM $Fe(CN)_6^{4-}$ under ~33 mW cm^{-2} of ENH-type W-halogen illumination.

(A) The n-Si/Gr electrodes from the batch Gr_A exhibited stable current densities for > 1000 s (5/5 stable). (B) The n-Si/F–Gr electrodes from batch F–Gr_B exhibited stable current densities for > 1000 s (5/5 stable). (C) The n-Si/Gr electrodes from batch Gr_C did not consistently exhibit stable current densities for > 1000 s (2/6 stable). (D) The n-Si/F–Gr electrodes from batch F–Gr_D exhibited stable current densities for > 1000 s (5/5 stable).

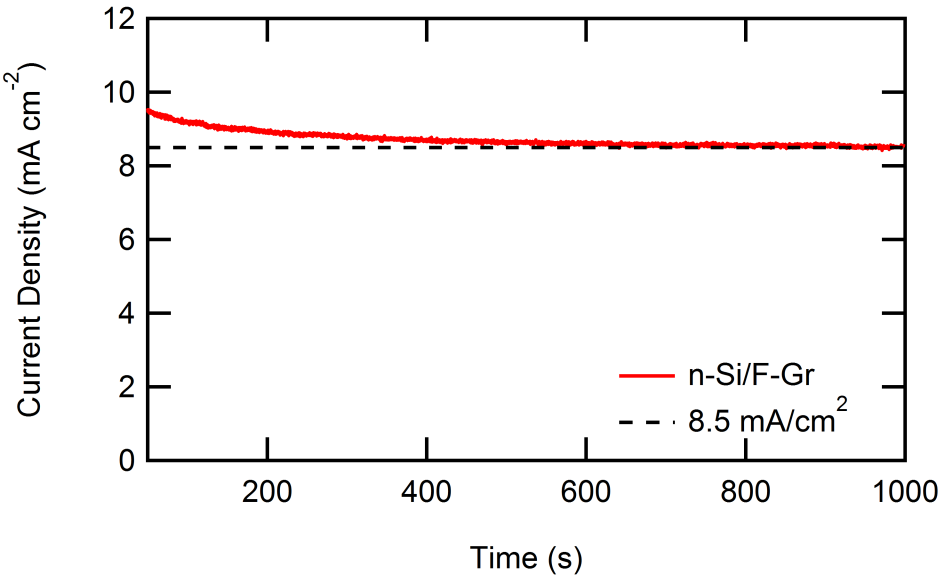

Figure S3. Representative *J-t* data of an n-Si/F–Gr electrode in contact with aqueous 50 mM $Fe(CN)_6^{3-}$ - 350 mM $Fe(CN)_6^{4-}$ under ~33 mW cm^{-2} of W-halogen illumination. After an initial decay in current density, the current density stabilized at ~8.5 mA cm^{-2}.

We also explored the extended stability behavior of the Gr-coated n-Si electrodes as compared to F–Gr-coated n-Si electrodes. Figure S4 depicts the *J-t* behavior of the most stable n-Si/F–Gr and n-Si/Gr electrodes. After both starting at an initial current density of ~10 mA cm^{-2}, the n-Si/F–Gr electrode current density decayed to 9.5 mA cm^{-2}, whereas the n-Si/Gr electrode decayed to 8 mA cm^{-2}. The fluorinated graphene-coated electrode was more stable, but the

pristine graphene coated electrode also exhibited stability, particularly between *t*=20,000 s and *t*=80,000 s. In conjunction with the data depicted in Figure S2, under ideal conditions for extended (100,000 s) time periods, these observations suggest that pristine graphene may be able to provide to n-Si electrodes the same level of stability as that provided by F–Gr coatings. However, some difficult-to-control variable in the growth or transfer of graphene limits the routine observation of such extended stability. This hypothesis is consistent with the supposition that grain boundaries and defect sites on the graphene coatings lead to the observed degradation, and that fluorination of such sites passivates them to further loss of integrity. Hence, the inconsistency seen in the graphene electrode stability data can be ascribed to the relative preponderance or dearth of defect sites present on an electrode surface, with fluorination greatly decreasing the effect that such sites have on the photoelectrochemical stability of such systems. Future work involving the targeted study of single crystal graphene sheets or single grains in a polycrystalline graphene sheet are underway to further examine this hypothesis.

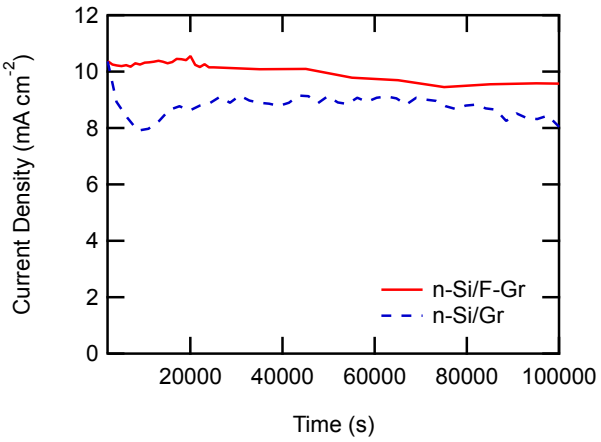

Figure S4. *J-t* data of the 'champion' n-Si/F–Gr and n-Si/Gr electrodes in contact with aqueous 50 mM $Fe(CN)_6^{3-}$ - 350 mM $Fe(CN)_6^{4-}$ under ~33 mW cm^{-2} of W-halogen illumination. After both starting at an initial current density of ~10 mA cm^{-2}, the n-Si/F–Gr electrode current density decayed to 9.5 mA cm^{-2} compared to the n-Si/Gr electrode which decayed to 8 mA cm^{-2}.

Stability of fluorinated graphene-covered n-Si electrodes under high light intensity conditions

Fluorinated graphene-coated and pristine graphene-coated n-Si electrodes were tested for photoelectrochemical stability under approximately 1 sun conditions (~100 mW cm^{-2} from an ENH-type W-halogen lamp). Figure S5 depicts the photoelectrochemical stability over 1000 s for n-Si/Gr and n-Si/F–Gr electrodes in contact with aqueous 50 mM $Fe(CN)_6^{3-}$ - 350 mM $Fe(CN)_6^{4-}$ under ~100 mW cm^{-2} of W-halogen illumination. The current density of the n-Si/F–Gr electrode was effectively constant over this time period, whereas the current density of the n-Si/Gr electrode decayed from ~25 mA cm^{-2} to less than 7 mA cm^{-2} over the same time period. This behavior supports the hypothesis that under these conditions fluorinated graphene provides a superior protective layer relative to pristine graphene. Figure S6 further depicts the photoelectrochemical stability under the same conditions of a F–Gr coated n-Si electrode over 100,000 s. Although the F–Gr coated electrode was stable over the same time period (100,000 s) under lower light intensity conditions (Figure 1), at near 1 sun conditions the current density of the electrode decayed to near baseline conditions over the same time period.

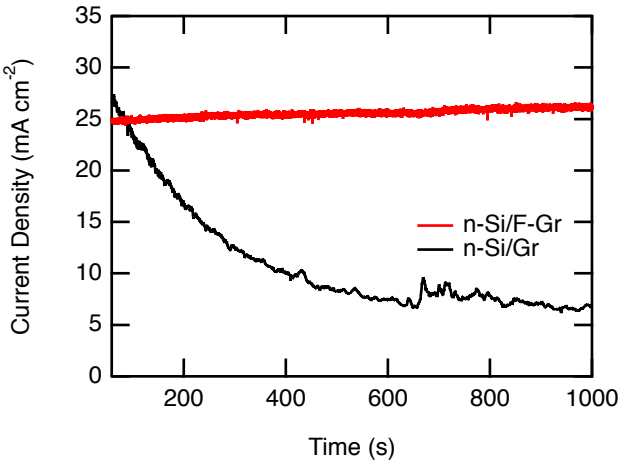

Figure S5. *J-t* data for n-Si/Gr and n-Si/F–Gr electrodes in contact with aqueous 50 mM $Fe(CN)_6^{3-}$ - 350 mM $Fe(CN)_6^{4-}$ under ~100 mW cm^{-2} of W-halogen illumination over 1000 s.

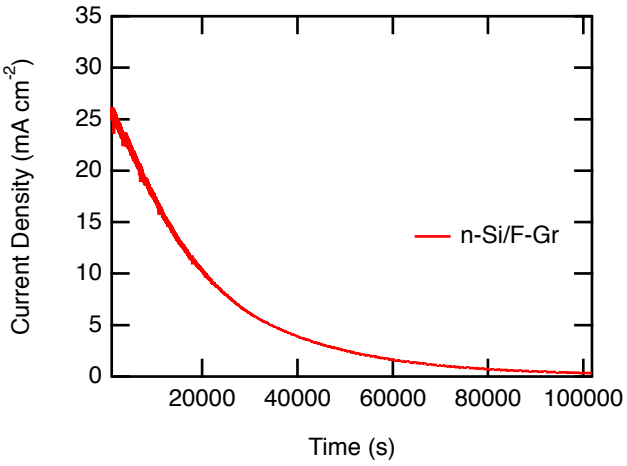

Figure S6. *J-t* data for n-Si/F–Gr electrodes in contact with aqueous 50 mM $Fe(CN)_6^{3-}$ - 350 mM $Fe(CN)_6^{4-}$ under ~100 mW cm^{-2} of W-halogen illumination over 100,000 s.

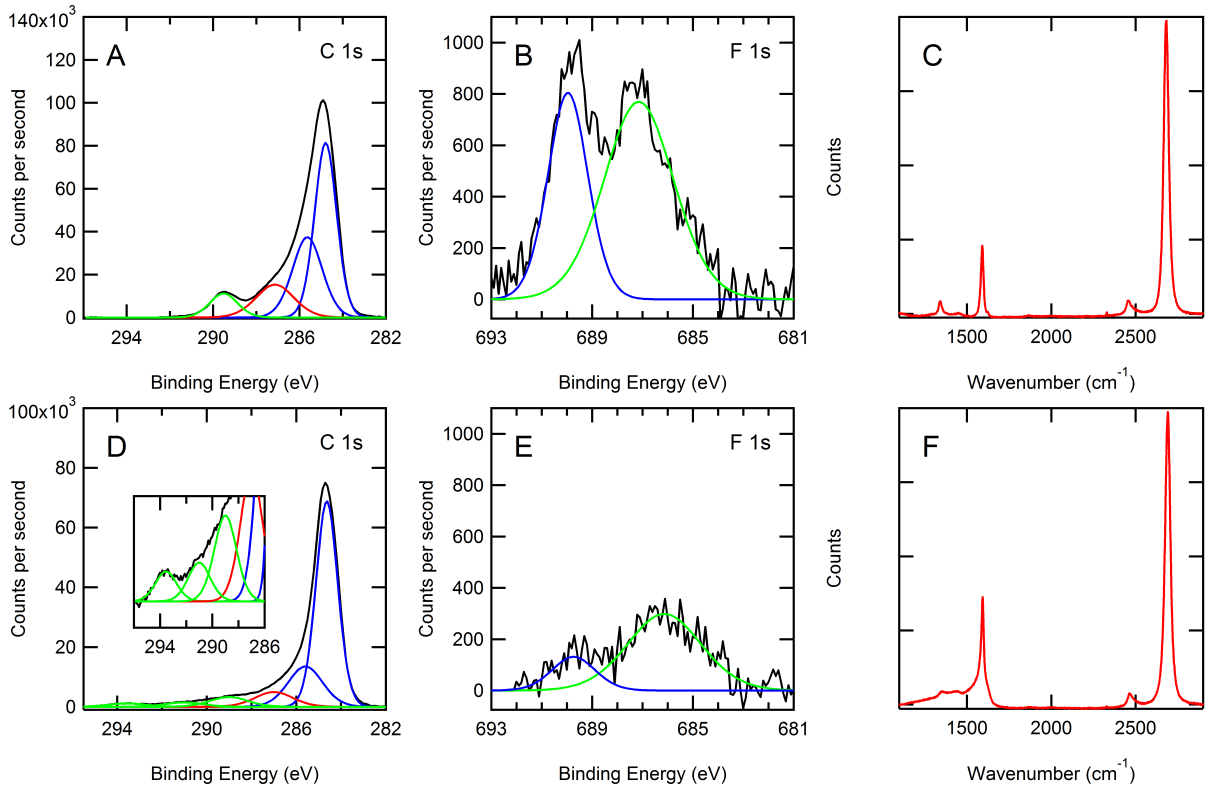

Figure S7. Raman and X-ray photoelectron spectra of fluorinated graphene (F–Gr) before and after annealing. (A) The C 1s region before annealing displayed four peaks at binding energies of 284.8 eV, 285.6 eV, 287.2 eV, and 289.5 eV, respectively. Peaks attributed to carbon bound to fluorine are shown in green; peaks attributed to carbon bound to carbon are shown in blue; and peaks attributed to carbon bound to oxygen are shown in red. (B) The F 1s region displayed two peaks at binding energies of 687.1 eV and 690.0 eV, respectively. (C) The Raman spectra before annealing showed a prominent defect peak at 1350 cm^{-1}. (D) Two additional peaks, at 291 eV and 293.5 eV (inset), attributable to CF_2 and CF_3 groups, were observed in the C 1s XP spectra after annealing. (E) The positions of the peaks in the F 1s region were shifted slightly to 686.1 eV and 689.8 eV, respectively, and decreased in size. (F) The defect peak at 1350 cm^{-1}

broadened after the anneal. These spectra are consistent with a lightly fluorinated (C_XF, x>10) graphene surface.[5] The change in fluorination profile after annealing is consistent with a reorganization of the fluorine on the surface, and the XPS spectra demonstrate the expected decrease in fluorine content after a two-hour 350 °C anneal under a H_2:Ar (5:95) atmosphere.[4]

Chemical stability of fluorinated graphene in aqueous solutions of varying pH (0,7,14)

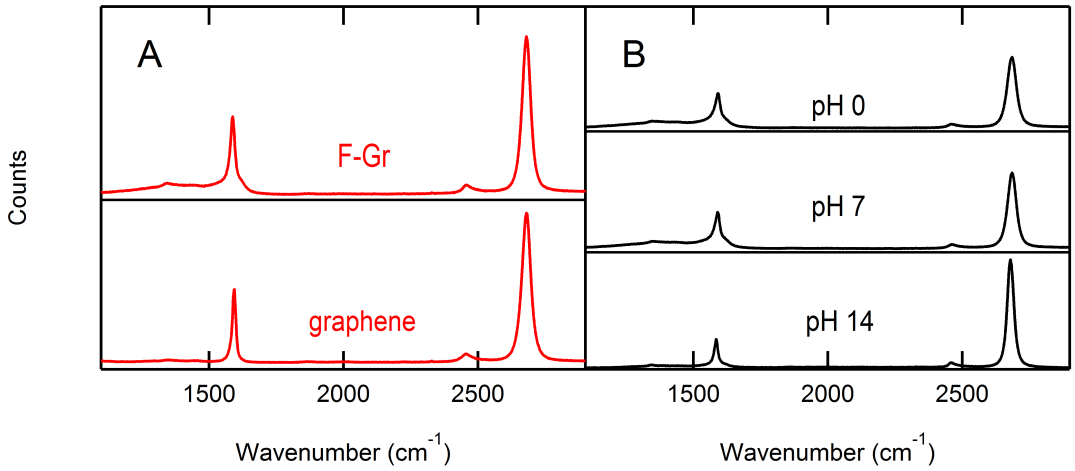

Figure S8. Stability tests of F–Gr in acidic (1 M HCl), alkaline (1 M KOH), and neutral aqueous conditions. (A) Raman spectra of the pristine graphene sheets before fluorination (bottom) and after fluorination (top) showed an increase in the size of the defect peak at 1350 cm^{-1}. (B) The 1350 cm^{-1} defect peak remained unchanged after 1 h in acidic or neutral aqueous solutions. In contrast, immersion for 1 h in aqueous alkaline media produced a decrease in the intensity of the defect peak. However, in all three spectra, the intensity of the G (~1580 cm^{-1}) and 2D (~2680 cm^{-1}) peaks are consistent with monolayer graphene.

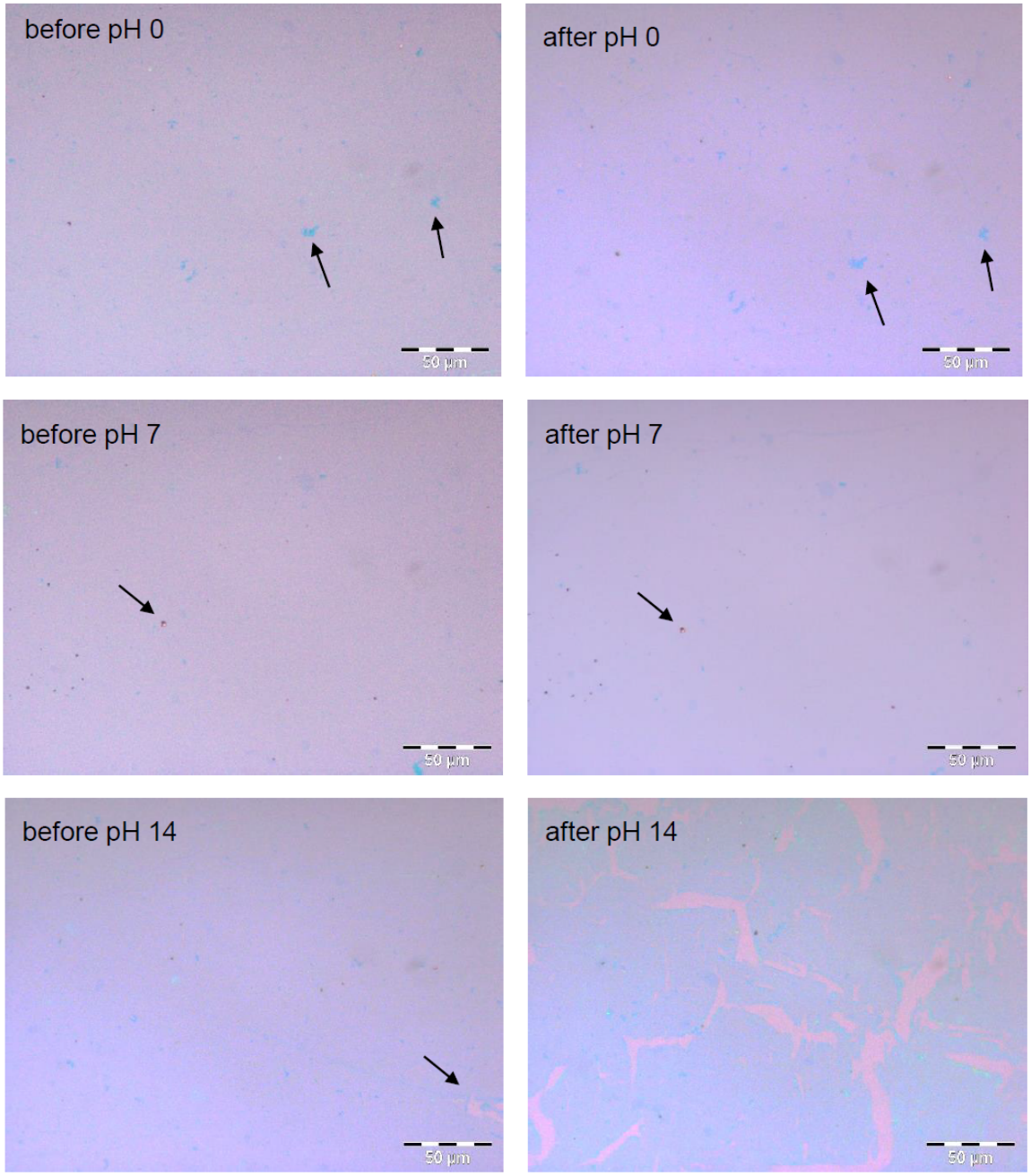

Figure S9. Optical images of stability tests of F–Gr in acidic (1 M HCl), alkaline (1M KOH), and neutral (deioninzed water) conditions. Arrows indicate points of reference for the corresponding before and after images.

The stability of the fluorinated graphene was tested under acidic, neutral, and alkaline aqueous solutions, respectively. To insure that the same area was examined before and after testing, a small area on the graphene wafer was outlined with Hysol 9460 epoxy. Optical images along with Raman spectra were acquired, and wafers were then placed for 1 h in aqueous solutions at pH 0, pH 7, and pH 14. After carefully rinsing the samples with >18 MΩ-cm H_2O and drying the samples with a stream of N_2(g), optical images along with Raman spectra were obtained from the same areas as before testing. The Raman spectra and optical images of the samples soaked in acidic and neutral solutions showed no change after testing (Figure S8-S9). The samples tested in alkaline solutions showed a marked decrease in defect density of the remaining sections of fluorinated graphene, closely mimicking the profile of pristine graphene. Repeated tests of fluorinated graphene in 1 M KOH(aq) showed large-scale delamination of the fluorinated graphene sheet, as observed in the images before and after exposure to the aqueous pH 14 solution.

UV/Vis spectroscopy of graphene and fluorinated graphene

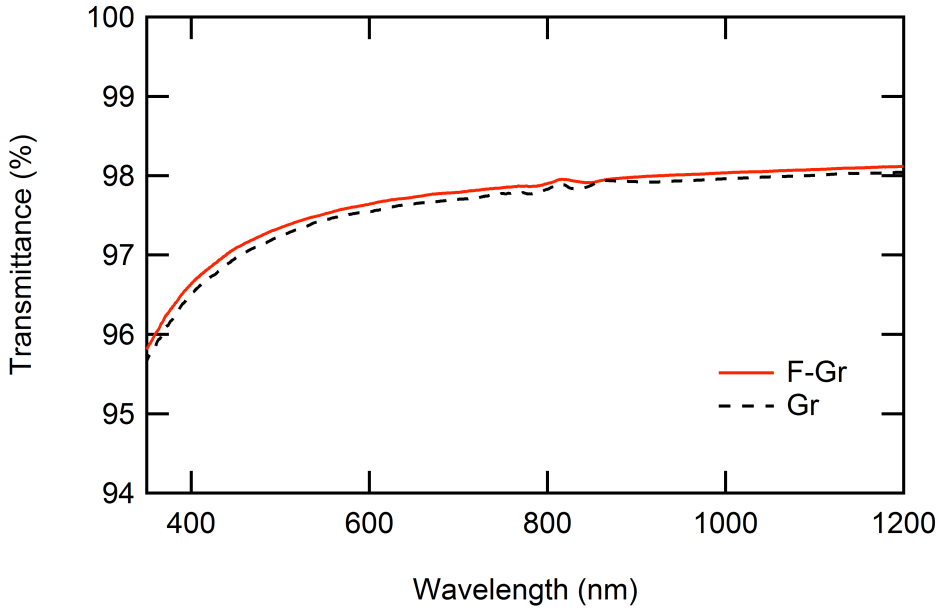

Figure S10. UV/Vis spectra of Gr and F–Gr on glass. Graphene and fluorinated graphene were transferred to borosilicate glass slides using the standard transfer procedures (see above). The slightly increased transmission for F–Gr is consistent with the expectation of decreased visible light absorption upon fluorination of graphene.

Inhibition of platinum silicide formation

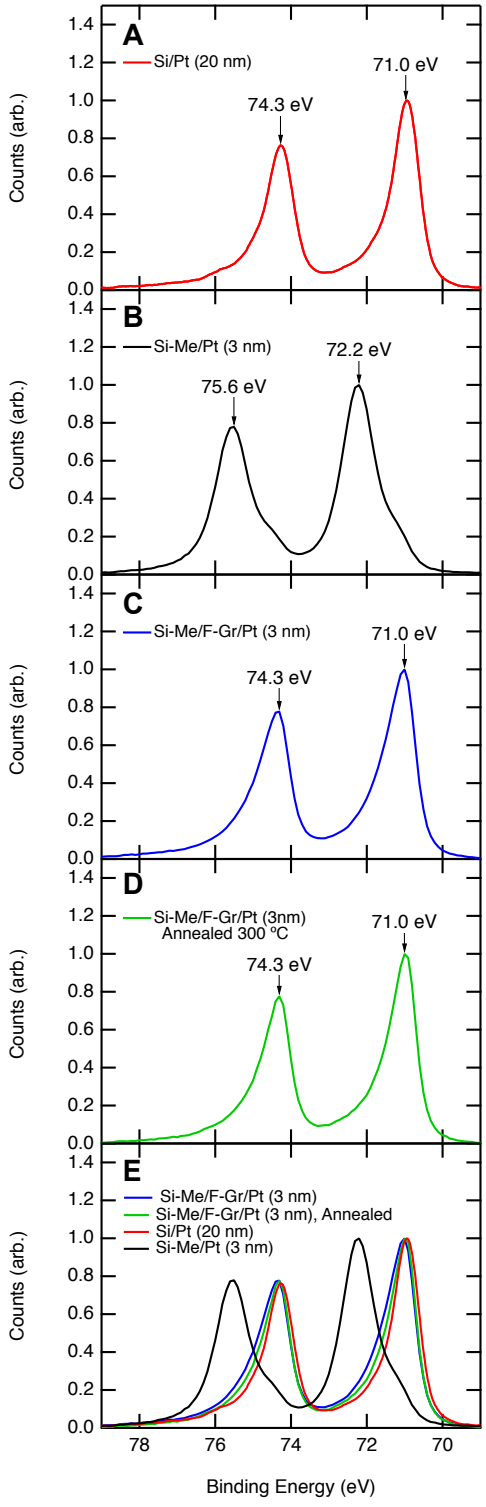

Figure S11. The Pt 4f XP spectra of Pt on both F–Gr covered and Si surfaces. (A) XP spectrum of a thick (20 nm) layer of Pt on Si. This spectrum is representative of a pure Pt phase. (B) XP spectrum of a 3 nm layer of Pt on Si. The Pt 4f peak shifted to higher binding energy (72.2 and 75.6 eV), characteristic of platinum silicide formation.[6] The shoulder to lower binding energy is attributed to a pure Pt phase. (C) XP spectrum of Si-Me/F–Gr/Pt (3 nm). The Pt 4f peak positions (71.0 and 74.3 eV) are consistent with pure Pt. (D) XP spectrum of Si-Me/F–Gr/Pt after annealing at 300 °C under forming gas. (E) Overlay of XP spectra (A)-(D).

XP spectra of Si-Me/F–Gr/Pt and Si-Me/Pt surfaces were obtained to investigate the ability of F–Gr to inhibit platinum silicide formation. Pt was deposited at ~3 nm thickness via electron-beam evaporation on both F–Gr covered and bare Si surfaces. The 3 nm Pt thickness was chosen to allow for

interrogation of the sample surface to a depth at which both Si and Pt ware observable by XPS. Methylated Si surfaces were used to inhibit the formation of Si oxide at the Si/Pt interface during sample fabrication, because Si oxide of sufficient thickness is also capable of preventing silicide formation.[7] Figure S11a shows the XP spectrum of a pure Pt phase. A thicker Pt layer (20 nm) was used to interrogate only the pure Pt phase. Figure S11b shows the Pt 4f XP spectrum of CH_3-terminated Si with a 3 nm Pt overlayer. The Pt 4f peak shifted to higher binding energy, indicative of platinum silicide formation.[6] The shoulder of the peaks at low binding energy is consistent with a pure Pt phase overlayer. Conversely, 3 nm of Pt on F–Gr covered silicon showed essentially no change in the Pt 4f binding energy immediately after fabrication (Figure S11c or after a 1 h anneal under forming gas at 300 °C (Figure S11d). The data are thus indicative of little or no platinum silicide formation. Figure S11e presents an overlay of the spectra in Figure S11a-S11d and highlights the difference between the Pt 4f peak positions.

N-Si/F–Gr nonaqueous photoelectrochemistry

Table S1. E_{oc} values for n-Si/Gr and n-Si/F–Gr electrodes in contact with non-aqueous redox couples under ~33 mW cm^{-2} of ENH-type W-halogen illumination. The Nernstian potential, $E(A/A^-)$, of the contacting non-aqueous electrolytes were measured as follows: $E(CoCp_2^{+/0}) = -1.26$ V vs. $E°'(Fc^{+/0})$, $E(Fc^{+/0}) = -0.1$ V vs. $E°'(Fc^{0/+})$, $E(AcFc^{+/0}) = +0.4$ V vs $E°'(Fc^{+/0})$.

	$E_{oc,CoCp2+/0}$ (V vs. $E(CoCp_2^{+/0})$)	$E_{oc,Fc+/0}$ (V vs. $E(Fc^{+/0})$)	$E_{oc,AcFc+/0}$ (V vs. $E(AcFc^{+/0})$)
Gr	0	0.26	0.43
F–Gr	0	0.20	0.30

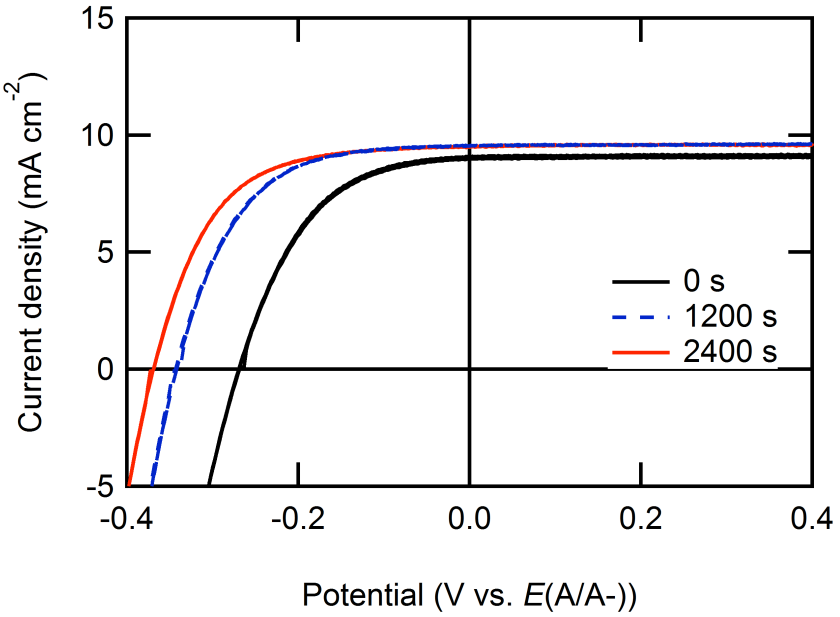

Figure S12. Current density-potential (*J-E*) behavior of an n-Si/F–Gr/Pt photoanode before, during, and after 2400 s of photoelectrochemical stability testing in contact with 0.4M Br_2 - 7.0 M HBr (pH=0) aqueous electrolyte. Photoelectrochemical stability was measured by observing the *J-t* behavior at an initial current density of 10 mA cm^{-2} over the specified time period (see Figure 3). The behavior of the n-Si/F–Gr/Pt electrode improved over 2400 s, with improvements in E_{oc} (0.27 V to 0.37 V), J_{SC} (9.0 mA to 9.5 mA), and *ff* (0.51 to 0.59), resulting in an increase in the ideal regenerative cell conversion efficiency from 3.5% to >5%.

XPS analysis of silicon oxide thickness

XPS analysis was performed in order to determine the effect of electrochemical oxidation at the Si–Me surface on the oxidation state of the Si photoanode surface (Figure 2). Silicon oxide detected before and after electrochemical oxidation was quantified using a simple substrate—overlayer model described by equation 1:[8]

$$d = \lambda_{ov} \sin\theta \left\{ \ln\left[1 + \frac{I^o_{Si}}{I^o_{ov}} * \frac{I_{ov}}{I_{Si}} \right] \right\} \quad (1)$$

where d is the overlayer thickness, λ_{ov} is the attenuation factor through the oxide overlayer (assumed to be 2.6 nm)[9], θ the angle from the surface of the sample to the detector (90°), $\frac{I^o_{Si}}{I^o_{ov}}$ is an instrument normalization factor related to the expected signal for a pure Si and a pure SiO_2 sample (taken to be 1.3 for this instrument), I_{ov} is the measured intensity of the silicon, and I_{ov} is the measured intensity of the silicon oxide overlayer. The thickness of a monolayer of oxide was taken to be 0.35 nm.[10] Negligible silicon oxide was detected on the bare methyl-terminated silicon surfaces prior to electrochemical oxidation (Figure 2a) and an oxide thickness of approximately 0.75 nm, or >2 monolayers of oxide, was observed after exposure of the Si–Me surface (Figure 2b) to the electrochemical oxidation conditions described in Figure 2. An oxide thickness of approximately 0.15±0.05 nm was detected on the Si–Me/F–Gr surfaces prior to electrochemical oxidation (Figure 2c) and an oxide thickness of approximately 0.17± 0.5 nm, was observed after exposure (Figure 2d) of the Si–Me/F–Gr surface to the electrochemical oxidation conditions described in Figure 2.

np⁺-Si solid state junction behavior

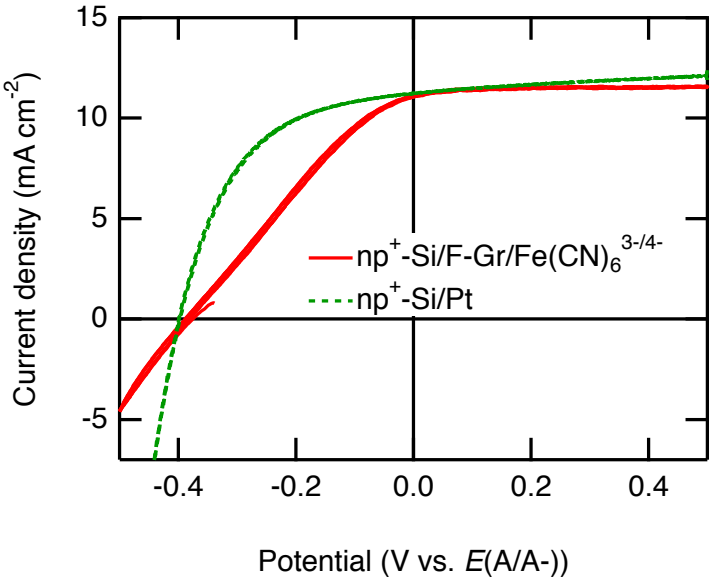

Figure S13. *J-E* behavior of an np⁺-Si/Pt PV cell and an np⁺-Si/F–Gr/$Fe(CN)_6^{3-/4-}$ photoanode under ~33 mW cm^{-2} of ENH-type W-halogen illumination. For the np⁺-Si/Pt PV cell, the following photovoltaic metrics were measured: E_{oc} = -0.40 V, J_{sc} = 11.3 mA cm^{-2}, *ff* = 0.50. For the np⁺-Si/F–Gr/$Fe(CN)_6^{3-/4-}$ cell, the following photovoltaic metrics were measured: E_{oc} = -0.39 V, J_{sc} = 11.1 mA cm^{-2}, *ff* = 0.30. The similar E_{oc} values with varying fill factors between these two interfaces suggest that the Si/F-Gr/$Fe(CN)_6^{3-/4-}$ interface is the source of an additional series resistance but that the parallel shunt resistances are similar between the np⁺-Si/Pt and np⁺-Si/F–Gr/$Fe(CN)_6^{3-/4}$ interfaces. A similar parallel shunt resistance is also consistent with the use of the same buried photoactive junction at each interface. The np⁺-Si/Pt PV cell was prepared by evaporating 15 nm of Pt onto the freshly HF etched p⁺ surface of an np⁺-Si chip and scribing a GaIn eutectic onto the backside of an n-doped surface. For the np⁺-Si/Pt PV cell, the (*E*(A/A-)) referenced on the x-axis refers to the potential of the Pt contact.

Analysis of fluorine atom concentration relative to defect site carbon concentration

A key hypothesis of this work is that the fluorination of CVD-grown graphene leads to passivation of defect sites present in CVD graphene. Assuming a carbon-carbon bond length of 0.142 nm and the hexagonal structure of graphene, the area of each hexagonal unit in a graphene sheet is 0.052 nm^2 and encompasses two carbon atoms. Therefore, *a 1 cm^2 sheet of pristine graphene will include ~ 1x10^{15} carbon atoms*. A rigorous evaluation of the density and total number of carbon atoms in a polycrystalline graphene sheet is challenging, due to the presence of a variety of defect types, including point and line defects, with various geometries, and also due to a variable number of defects that may be produced by fabrication of the graphene-covered electrode.[11] For simplicity, *we consider only the line defects associated with grain boundaries*. These line defects have a variety of geometries and can be composed of alternating 5- and 7-membered carbon rings. Assuming that the density of carbon atoms at a line defect and in the defect-free graphene sheet are equivalent, and further that *the density of carbon atoms in a polycrystalline CVD graphene sheet is equivalent to that in a single crystalline graphene sheet,* allows calculation of the percentage of total carbon atoms at defect sites in the graphene sheet. The grain size of the graphene used in this work is 0.2-5 μm on a side. The grains are generally amorphously shaped, but are approximated herein as hexagons for simplicity. Assuming hexagonal grains with side length of 0.2 μm (area of 0.10 μm^2) implies ~ 10^9 grains in a 1 cm^2 sheet of graphene, and a total length of 8 x 10^8 μm of grain boundary area. If the width of these boundaries is equal to the width of a single hexagonal unit of the graphene lattice (~0.28 nm), and assuming that the carbon density is the same as that of a single hexagonal unit, the total number of defect carbon atoms at grain boundary line defects is ~10^5 C atoms per 1 cm^2 area of graphene. Thus (10^5/10^{15}), i.e., 1 defective carbon atom is present for every 10^{10} pristine carbon

atoms in the polycrystalline graphene sheet. This ratio is significantly smaller than the ratio of F atoms to C atoms found via XPS analysis ($10 > F/C > 0.01$. In conjunction with the expectation that the defect sites on a graphene sheet are significantly more reactive than the pristine carbon sites, this XPS F/C ratio suggests that most or all of the defect carbon atoms are capped with fluorine. Further studies using electron microscopy methods are underway to confirm this hypothesis.

SEM of Pt electrodeposition on n-Si/F–Gr surfaces

Assuming 100% faradaic yield for charge transfer to platinum during the photoelectrochemical deposition of Pt from an aqueous solution of 5 mM K_2PtCl_4 and 200 mM LiCl, in conjunction with 2 e- per Pt atom deposited, and a conformal deposition, a charge density of -100 mC cm^{-2} should result in the deposition of a ~50 nm thick of Pt layer on the n-Si/F–Gr electrodes. SEM images were obtained on n-Si/F–Gr surfaces before photoelectrochemical deposition and after 10 mC cm^{-2} or 100 mC cm^{-2} of cathodic charge density was passed during electrodeposition (Figure S14-S16). Figure S15 indicates that the Pt deposited stochastically across the F–Gr surface, in contrast to previous reports of metal deposition via other methods on graphene, which produced preferential metal deposition at grain boundaries.[12] This difference in behavior may be due to passivation of highly reactive grain boundary sites by the XeF_2 treatment. The incomplete electrochemical stability observed in Figure 3 for the n-Si-H/Pt electrode may be related to imperfect conformal deposition, consistent with the observations of Figure S16.

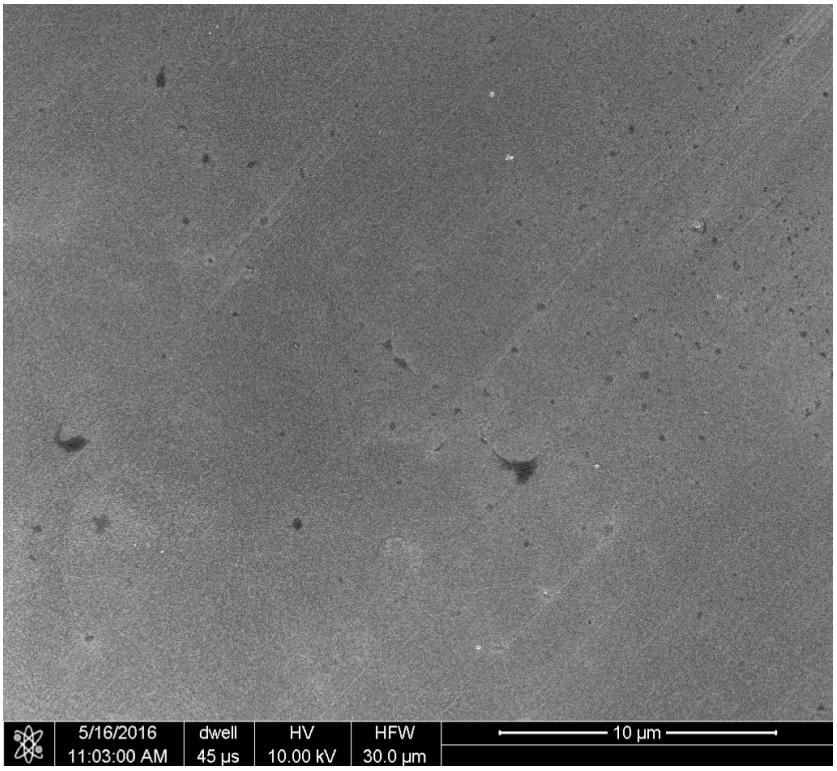

Figure S14. SEM image of a fluorinated graphene-covered n-Si surface prior to photoelectrochemical deposition of Pt metal from an aqueous solution of 5 mM K_2PtCl_4 (99.9%, Alfa Aesar) and 200 mM LiCl.

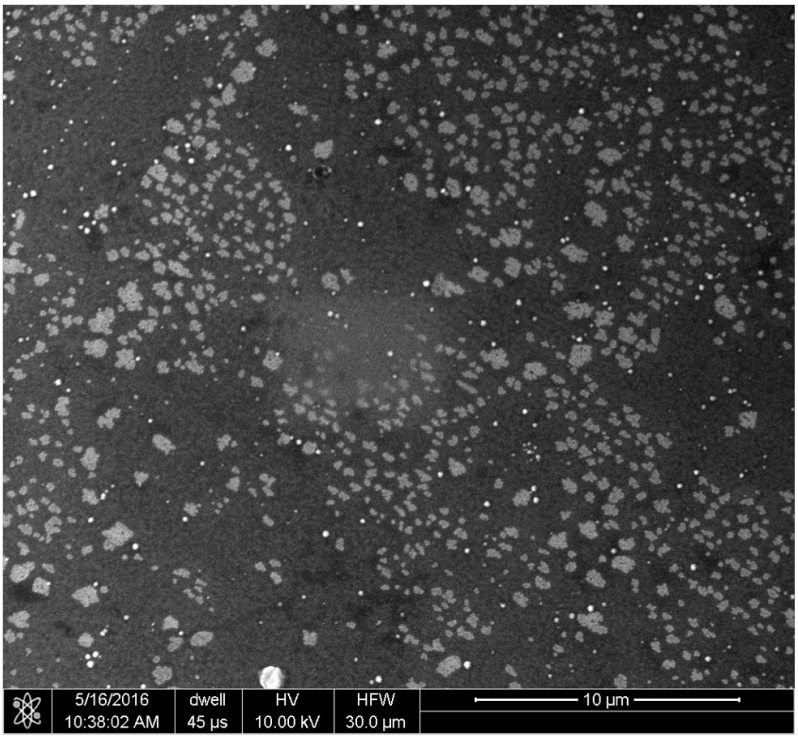

Figure S15. SEM image of a fluorinated graphene-covered n-Si surface after passing 10 mC cm^{-2} charge during photoelectrochemical deposition of Pt metal from an aqueous solution of 5 mM K_2PtCl_4 (99.9%, Alfa Aesar) and 200 mM LiCl.

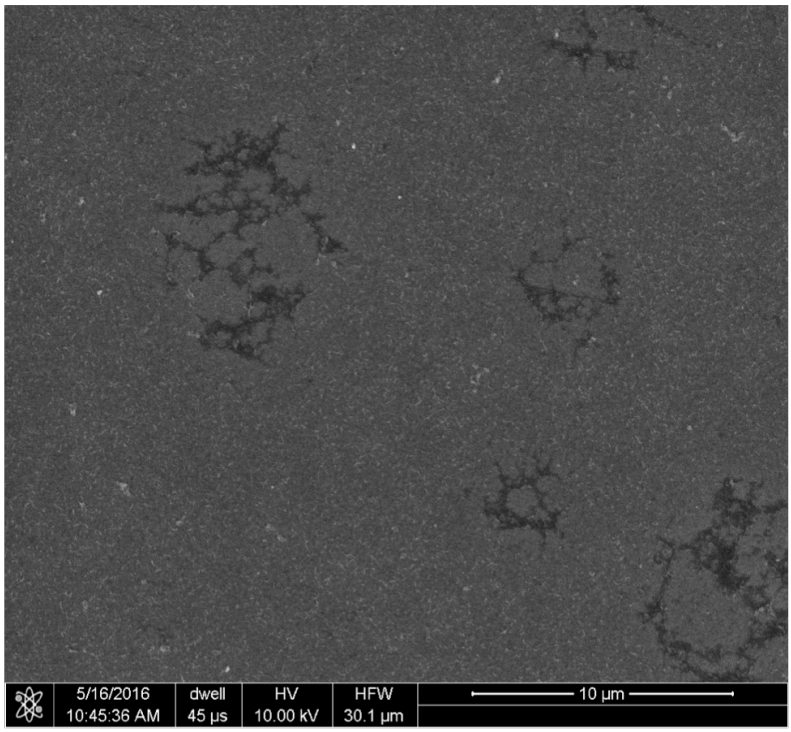

Figure S16. SEM image of a fluorinated graphene-covered n-Si surface after passing 100 mC cm^{-2} charge during photoelectrochemical deposition of Pt metal from an aqueous solution of 5 mM K_2PtCl_4 (99.9%, Alfa Aesar) and 200 mM LiCl.

III. References

1. Yang, J.; Walczak, K.; Anzenberg, E.; Toma, F. M.; Yuan, G.; Beeman, J.; Schwartzberg, A.; Lin, Y.; Hettick, M.; Javey, A.; Ager, J. W.; Yano, J.; Frei, H.; Sharp, I. D. *J. Am. Chem. Soc.* **2014,** 136, (17), 6191-6194.

2. Petrone, N.; Dean, C. R.; Meric, I.; van der Zande, A. M.; Huang, P. Y.; Wang, L.; Muller, D.; Shepard, K. L.; Hone, J. *Nano Lett.* **2012,** 12, (6), 2751-2756.

3. Pirkle, A.; Chan, J.; Venugopal, A.; Hinojos, D.; Magnuson, C. W.; McDonnell, S.; Colombo, L.; Vogel, E. M.; Ruoff, R. S.; Wallace, R. M. *Appl. Phys. Lett.* **2011,** 99, (12), -.

4. Plymale, N. T.; Kim, Y.-G.; Soriaga, M. P.; Brunschwig, B. S.; Lewis, N. S. *J. Phys. Chem. C* **2015,** 119, (34), 19847-19862.

5. Stine, R.; Lee, W.-K.; Whitener, K. E.; Robinson, J. T.; Sheehan, P. E. *Nano Lett.* **2013,** 13, (9), 4311-4316.

6. Larrieu, G.; Dubois, E.; Wallart, X.; Baie, X.; Katcki, J. *J. Appl. Phys.* **2003,** 94, (12), 7801.

7. Abelson, J. R.; Kim, K. B.; Mercer, D. E.; Helms, C. R.; Sinclair, R.; Sigmon, T. W. *J. Appl. Phys.* **1988,** 63, (3), 689-692.

8. Briggs, D.; Seah, M. P., *Practical Surface Analysis*. 2nd ed.; John Wiley & Sons Ltd: Chichester, England, 1990.

9. Hochella Jr, M. F.; Carim, A. H. *Surf. Sci.* **1988,** 197, (3), L260-L268.

10. Haber, J. A.; Lewis, N. S. *J. Phys. Chem. B* **2002,** 106, (14), 3639-3656.

11. Banhart, F.; Kotakoski, J.; Krasheninnikov, A. V. *ACS Nano* **2011,** 5, (1), 26-41.

12. Kim, K.; Lee, H.-B.-R.; Johnson, R. W.; Tanskanen, J. T.; Liu, N.; Kim, M.-G.; Pang, C.; Ahn, C.; Bent, S. F.; Bao, Z. *Nat Commun* **2014,** 5.